

## Research Article

# Nanocomposite of CeO<sub>2</sub> and High-Coercivity Magnetic Carrier with Large Specific Surface Area

Alice Reznickova Mantlikova,<sup>1</sup> Jiri Plocek,<sup>2</sup> Barbara Pacakova,<sup>1</sup> Simona Kubickova,<sup>1</sup> Ondrej Vik,<sup>2</sup> Daniel Niznansky,<sup>3</sup> Miroslav Slouf,<sup>4</sup> and Jana Vejpravova<sup>1</sup>

<sup>1</sup>Department of Magnetic Nanosystems, Institute of Physics of the CAS, v.v.i., Na Slovance 2, 182 21 Prague 8, Czech Republic

<sup>2</sup>Institute of Inorganic Chemistry of the CAS, v.v.i., Husinec-Rez 1001, 250 68 Rez, Czech Republic

<sup>3</sup>Department of Inorganic Chemistry, Faculty of Science, Charles University in Prague, Hlavova 2030/8, 128 43 Prague 2, Czech Republic

<sup>4</sup>Institute of Macromolecular Chemistry, Academy of Sciences of the Czech Republic, Heyrovsky Sq. 2, 162 06 Prague 6, Czech Republic

Correspondence should be addressed to Jana Vejpravova; vejpravo@fzu.cz

Received 26 August 2016; Revised 27 October 2016; Accepted 13 November 2016

Academic Editor: Mohamed Bououdina

Copyright © 2016 Alice Reznickova Mantlikova et al. This is an open access article distributed under the Creative Commons Attribution License, which permits unrestricted use, distribution, and reproduction in any medium, provided the original work is properly cited.

We succeeded in the preparation of CoFe<sub>2</sub>O<sub>4</sub>/CeO<sub>2</sub> nanocomposites with very high specific surface area (up to 264 g/m<sup>2</sup>). First, highly crystalline nanoparticles (NPs) of CoFe<sub>2</sub>O<sub>4</sub> (4.7 nm) were prepared by hydrothermal method in water-alcohol-oleic acid system. The oleate surface coating was subsequently modified by ligand exchange to citrate. Then the NPs were embedded in CeO<sub>2</sub> using heterogeneous precipitation from diluted Ce<sup>3+</sup> sulphate solution. Dried samples were characterized by Powder X-Ray Diffraction, Energy Dispersive X-Ray Analysis, Scanning and Transmission Electron Microscopy, Mössbauer Spectroscopy, and Brunauer-Emmett-Teller method. Moreover, detailed investigation of magnetic properties of the bare NPs and final composite was carried out. We observed homogeneous embedding of the magnetic NPs into the CeO<sub>2</sub> without significant change of their size and magnetic properties. We have thus demonstrated that the proposed synthesis method is suitable for preparation of extremely fine CeO<sub>2</sub> nanopowders and their nanocomposites with NPs. The morphology and magnetic nature of the obtained nanocomposites make them a promising candidate for magneto-responsive catalysis.

## 1. Introduction

Nanocomposites composed of nanoparticles (NPs) incorporated in functional matrix, which combine more than one functional physical and/or chemical property, are suggested as promising candidates for applications in various fields such as biomedicine, catalysis, and data storage [1–4]. In the last decade, several nanomaterials with magnetic and catalytic functionalities have been developed. Catalytic materials in form of NPs exhibit increase of the catalytic activity and number of active sites accessible for the reaction in comparison to the bulk counterparts due to the large surface-to-volume ratio and enhanced reactivity of the molecular orbitals of the surface species [5]. By incorporation of magnetically active components, the nanomaterials could be used as magnetically

separable catalysts for various applications requiring effective and rapid separation of the active substance from liquid phase [5–9]. This is very beneficial for the solution of the environmental problems such as the wastewater treatment [9].

Cerium oxide, CeO<sub>2</sub>, is one of the most important catalytic materials [10–12]. It exhibits relatively high catalytic activity under UV and visible light irradiation, sufficient chemical stability, and nontoxicity. Also its two special features—high reactivity mediated by the redox couple Ce<sup>IV</sup>/Ce<sup>III</sup> and exceptional oxygen storage capacity [13]—make this material unique. CeO<sub>2</sub>-containing materials are often used in industry [12] as components of commercial catalysts for reduction of the CO, hydrocarbons and NO<sub>x</sub> emissions from gasoline engines [14], and fuel cell technologies

[15], in wastewater treatment [16], and in cadmium [17] or lead [18] removal. Creation of the nanocomposite systems comprising the  $\text{CeO}_2$  and magnetic NPs could extend possible applications of this material [19]. For example, the  $\text{CuFe}_2\text{O}_4/\text{CeO}_2$  nanocomposite is a promising material in energy storage [20];  $\text{Fe}_3\text{O}_4/\text{CeO}_2$  was identified as magnetically separable catalyst [21, 22].

The use of magnetite as a magnetic carrier may be problematic by its instability against topotactic oxidation to maghemite [23, 24] and transformation to hematite at elevated temperatures [25, 26], which are often unavoidable for proper functionality of the catalyst. Therefore,  $\text{CoFe}_2\text{O}_4$  is a suitable magnetic material due to its high magnetic anisotropy, relatively high saturation magnetization ( $80 \text{ Am}^2 \text{ kg}^{-1}$  [27]) and coercivity (up to 2 T at low temperatures for NPs in the matrix [28]), good mechanical hardness, and excellent chemical stability against oxidation [28, 29]. Use of the  $\text{CoFe}_2\text{O}_4$  as catalyst [30, 31] or magnetic carrier for magnetically separable catalysts based on activated carbon [9],  $\text{TiO}_2$  [32], or  $\text{ZnO}$  [33] was reported recently.  $\text{CoFe}_2\text{O}_4/\text{CeO}_2$  nanocomposite should be a very promising candidate as a magnetic separable catalyst.

Up to date, only little work has been done on the preparation and characterization of the  $\text{CoFe}_2\text{O}_4\text{-CeO}_2$  system. Wetchakun et al. report on successful preparation of the  $\text{CoFe}_2\text{O}_4/\text{CeO}_2$  composite by coupling homogeneous precipitation with hydrothermal method [34]. The particle size and specific surface area were controlled by  $\text{CoFe}_2\text{O}_4$  to  $\text{CeO}_2$  ratio.

Recently, we have introduced a general approach for the preparation of multifunctional nanocomposites of monodisperse NPs embedded in oxide matrices [35]. This method enabled homogenous embedding of the  $\text{CoFe}_2\text{O}_4$  NPs into various oxide matrices without change of the NP diameter and size distribution and their magnetic response. Unfortunately, this method was not successful in the case of the  $\text{CeO}_2$  matrix due to the problematic hydrolysis of the cerium alkoxides. Therefore, we have modified this approach by excluding the alkoxides and successfully prepared the  $\text{CoFe}_2\text{O}_4/\text{CeO}_2$  nanocomposites by embedding the NPs with the help of heterogeneous precipitation of the  $\text{CeO}_2$  matrix at basic pH.

Using the modified approach, we have prepared a series of  $\text{CoFe}_2\text{O}_4/\text{CeO}_2$  nanocomposite samples varying the conditions of the incorporation of the NPs into the matrix. We have paid a special attention to identify the exact specific preparation conditions leading to the minimal change of the embedded  $\text{CoFe}_2\text{O}_4$  NPs properties together with the best potential catalytic activity of the  $\text{CeO}_2$  matrix. The successful embedding of the  $\text{CoFe}_2\text{O}_4$  NPs into the  $\text{CeO}_2$  matrix was confirmed for all samples. Magnetic response of the matrix-free modified sample and nanocomposites was compared with that of the bare  $\text{CoFe}_2\text{O}_4$  NPs, which enabled classifying any changes of the NP properties after their surface modification and insertion into the matrix. The role of the preparation conditions in the structure and magnetic response of the individual  $\text{CoFe}_2\text{O}_4$  NPs has been studied. Also the structure, morphology, and specific surface areas of

the nanocomposites were examined carefully. The proposed preparation route can be easily scaled up and modified for systems with more components or doped materials.

## 2. Materials and Methods

**2.1. Preparation.** We designed a two-step synthesis for preparation of the  $\text{CoFe}_2\text{O}_4/\text{CeO}_2$  nanocomposites. First, the oleic acid coated  $\text{CoFe}_2\text{O}_4$  NPs were obtained by the hydrothermal synthesis in the presence of oleic acid as was reported previously [29, 35]. The reference as-prepared matrix-free sample was obtained by drying the ferrofluid at  $75^\circ\text{C}$  and labeled as  $\text{CoFe}_{\text{free}}$ .

The hydrophobic NPs (dispersed in hexane) are unsuitable for the reaction in the aqueous media, which is essential for their incorporation into the  $\text{CeO}_2$  matrix. Hence the surface modification of the NPs was done by citric acid. After that, the NPs were incorporated into the matrix. Preparation conditions, such as the final pH or method of its adjustment, were varied for each sample in order to reach optimal morphology of the nanocomposite.

**2.1.1. Citrate Surface Modification of the  $\text{CoFe}_2\text{O}_4$  NPs.** Surface modification of the  $\text{CoFe}_2\text{O}_4$  NPs was inspired by methods described in [36–38]. First, 100 mL of acetone was added to the 10 mmol  $\text{CoFe}_2\text{O}_4$ -hexane solution. The precipitate was magnetically separated and the liquid was decanted afterwards—this procedure was repeated two times. The separated precipitate was dispersed in 100 mL of water, and then 1.5 mL of concentrated nitric acid together with 40 mmol of citric acid was added. The reaction mixture was heated at  $80^\circ\text{C}$  under simultaneous sonication in ultrasonic bath (at 80 W transferred power) for 90 min. After cooling the mixture to room temperature (RT), the modified  $\text{CoFe}_2\text{O}_4$  NPs were purified by combination of resuspension in acetone (3x) and diethylether (2x) and magnetic separation of the NPs. The purified NPs were dispersed in 100 mL of water and sonicated for 15 h. The final water dispersion was stable for more than 6 months at RT. We also tested pH-influence on stability of the citrate modified  $\text{CoFe}_2\text{O}_4$  NPs in water solution. The sample was stable in the pH range of 2.4–13.0 for few hours. Amount of the citric acid coating was determined gravimetrically by Thermogravimetry-Differential Thermal Analysis (TG-DTA). The reference matrix-free modified sample, labeled as  $\text{CoFe}_{\text{mod}}$ , was obtained by drying the ferrofluid at  $45^\circ\text{C}$ .

**2.1.2. Embedding of the ( $\text{CoFe}_2\text{O}_4$ ) NPs into the ( $\text{CeO}_2$ ) Matrix.** General procedure starts with 5 mmol solution of cerium sulphate in 150 mL of distilled water with 2 mL of concentrated sulfuric acid (solution A). This solution was diluted to 750 mL with distilled water and then pH was set to 2.6 by addition of 0.5 M sodium hydroxide solution. In the next step, solution of 0.5 mmol citrate modified  $\text{CoFe}_2\text{O}_4$  NPs was added to 250 mL of water (solution B). Solution B was stirred and sonicated (at 200 W transferred power) for 30 min. Afterwards, pH was set to 3.5 by addition of diluted sulfuric acid (1:5). Solutions A and B were mixed together

TABLE 1: Specific preparation conditions of the  $\text{CoFe}_2\text{O}_4/\text{CeO}_2$  nanocomposite samples together with the results of the PXRD (particle size,  $d_{\text{XRD}}^{\text{CeO}_2}$ , with range of error  $\sim 0.5$  nm and lattice parameter,  $a^{\text{CeO}_2}$ , of the  $\text{CeO}_2$  phase with range of error  $\sim 0.01$  Å) and catalytic (specific surface area measured by BET method,  $S_{\text{BET}}$ ) measurements.

Sample	Final pH	pH adjustment method	$d_{\text{XRD}}^{\text{CeO}_2}$ (nm)	$a^{\text{CeO}_2}$ (Å)	$S_{\text{BET}}$ ( $\text{m}^2/\text{g}$ )
v02	6	Dropwise addition of NaOH	2.3	5.42	$132 \pm 4$
v03	8	Dropwise addition of NaOH	2.1	5.42	$176 \pm 5$
v04	10	Dropwise addition of NaOH	1.7	5.42	$190 \pm 6$
v05	10	Fast addition of NaOH	1.8	5.41	$189 \pm 6$
v06	12	Fast addition of NaOH	1.7	5.42	$264 \pm 8$

and stirred for 15 min under continuous sonication (at 20 W transferred power, 10% duty cycle, 5 min).

Furthermore, 0.5 M sodium hydroxide solution with the final pH value was added and method of pH adjustment varied for each prepared sample as summarized in Table 1. During neutralization, the mixture became turbid at pH around 5. After targeting the final pH value, the samples were heated at  $60^\circ\text{C}$  under intensive overnight stirring. pH slightly decreased during the heating; thus it was necessary to add small amount of sodium hydroxide for several times to keep the final pH value constant.

After cooling to RT the mixtures were decanted and then purified according to the following procedure: samples were redispersed in 750 mL of water by sonication, then decanted, and centrifuged. Afterwards, the samples were dispersed in 60 mL of water and centrifuged for three more times. The same procedure was performed with ethanol (2x) and finally with diethylether (1x). The samples kept under vacuum were finally heated at a rate of  $0.2^\circ\text{C}/\text{min}$  to  $200^\circ\text{C}$  and kept at final temperature for 2 h. The labels of the samples and details of preparation conditions are summarized in Table 1.

**2.2. Sample Characterization.** All samples were characterized using the RT Powder X-Ray Diffraction (PXRD) performed on the Philips X'Pert PRO MPD X-ray diffraction system equipped with the X'Celerator detector working with the  $\text{Cu-K}\alpha$  ( $\lambda = 1.5418$  Å; matrix-free samples) or  $\text{Co-K}\alpha$  ( $\lambda = 1.7889$  Å; nanocomposite samples) radiation. The high-temperature measurements were done in the same equipment (with the  $\text{Cu-K}\alpha$  radiation) accompanied by the high-temperature chamber in the temperature range of  $200$ – $500^\circ\text{C}$ . The particle size,  $d_{\text{XRD}}$ , was determined using the Rietveld refinement procedure implemented within the FullProf software [39].

The content of citric acid was determined gravimetrically by TG-DTA using a TG-DTA device by SETARAM. The Transmission Electron Microscopy (TEM) and High-Resolution TEM (HR-TEM) using TEM FEI Tecnai G2 Spirit and HR-TEM JEOL JEM 3010 (matrix-free samples, v02 and v06 nanocomposite samples) were performed in order to study the morphology of the prepared nanocomposites and possible determination of the particle size of the  $\text{CoFe}_2\text{O}_4$  NPs. TEM analysis was supplemented with selected area electron diffraction (TEM/SAED) and energy dispersive analysis of X-rays (TEM/EDX). The experimental TEM/SAED patterns were processed by program ProcessDiffraction [40] and

compared with the theoretical PXRD patterns of  $\text{CoFe}_2\text{O}_4$  and  $\text{CeO}_2$  using Crystallography Open Database [41] and program PowderCell [42] as described elsewhere [43].

The chemical composition of the samples was verified by Energy Dispersive X-Ray Analysis (EDX) using the Bruker Quantax EDS detector implemented within the Scanning Electron Microscope (SEM) Tescan Mira 3 LMH. The specific surface area of the samples was measured using Brunauer-Emmett-Teller (BET) nitrogen adsorption using the Quantachrome Instrument NOVA 4200e apparatus. Before the measurements, the samples were degassed at  $100^\circ\text{C}$  for 24 h.

The Mössbauer Spectroscopy measurement was done in transmission mode with  $^{57}\text{Co}$  diffused in the Rh matrix as the source moving with constant acceleration. The spectrometer (Wissel, Germany) was calibrated by standard  $\alpha\text{-Fe}$  foil and the isomer shift was related to this standard at 293 K. The resulting parameters were determined in the NORMOS program.

The magnetic measurements were carried out using the SQUID magnetometer (MPMS7XL, Quantum Design). The zero-field-cooled (ZFC) and field-cooled (FC) curves were recorded as follows: at first, the sample was cooled down to 10 K; then the magnetic field of 0.01 T was applied and the temperature dependence of the magnetization was measured up to 400 K (ZFC curve). Afterwards, the sample was cooled down to 10 K in the applied field and the FC curve was obtained. The magnetization isotherms (field dependence of the magnetization,  $M(B)$  curves) were measured at 10, 300, and 400 K up to the 7 T in both polarities. Distributions of magnetic moment values,  $\mu$ , of the  $\text{CoFe}_2\text{O}_4$  NPs were determined by analyzing the unhysteretic magnetization isotherms in the MINORIM software [44].

### 3. Results and Discussion

**3.1. Characterization of the Structure, Phase Composition, and Morphology.** The phase composition of the samples was studied using PXRD. Also the particle size of the  $\text{CoFe}_2\text{O}_4$  (for the matrix-free NPs in the  $\text{CoFe}_{\text{free}}$  and  $\text{CoFe}_{\text{mod}}$  samples only) and  $\text{CeO}_2$  was determined. The diffraction patterns of the  $\text{CoFe}_{\text{free}}$  and  $\text{CoFe}_{\text{mod}}$  samples exhibit only reflections corresponding to the  $\text{CoFe}_2\text{O}_4$  spinel phase (PDF database, card number 00-022-1086), with the lattice parameter  $a = (8.41 \pm 0.01)$  Å for both samples (Figure 1(a)). The crystalline size (size of coherently diffracted domain) determined by Rietveld refinement is  $d_{\text{XRD}}^{\text{CoFe}_{\text{free}}} = (4.7 \pm$

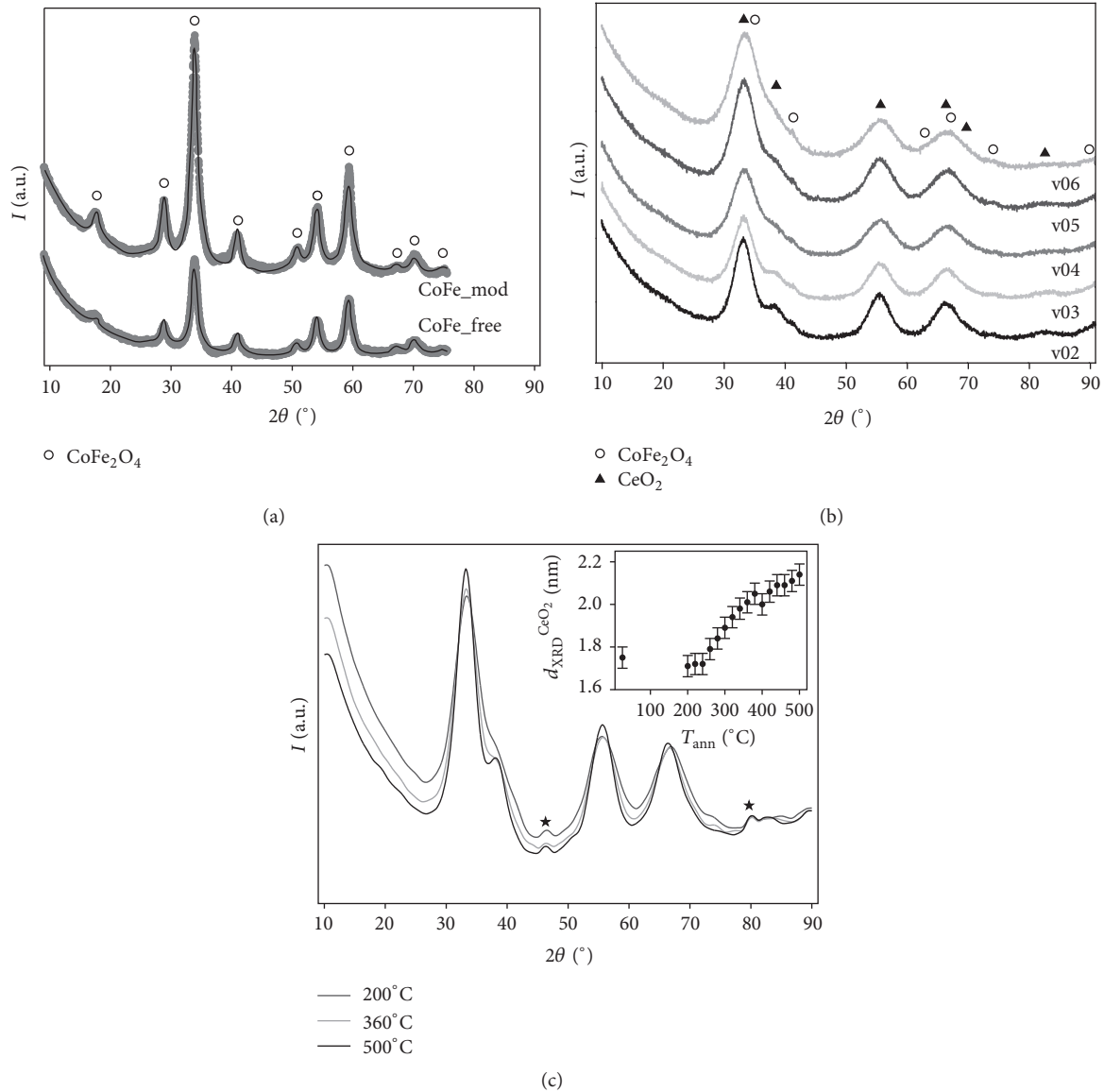


FIGURE 1: (a) The measured PXRD patterns of the matrix-free samples (Cu-K $\alpha$  radiation used) with the corresponding refined patterns (full black lines). (b) The measured PXRD patterns of the CoFe<sub>2</sub>O<sub>4</sub>/CeO<sub>2</sub> nanocomposite samples (Co-K $\alpha$  radiation used). White circles and black triangles indicate the Bragg positions corresponding to the CoFe<sub>2</sub>O<sub>4</sub> (PDF database, card number 00-022-1086) and CeO<sub>2</sub> (PDF database, card number 01-081-0792), respectively. (c) The examples of the high-temperature PXRD patterns of the v04 sample. Stars correspond to the reflections from the platinum heating strip. The dependence of the  $d_{\text{XRD}}^{\text{CeO}_2}$  on the  $T_{\text{ann}}$  with the corresponding error bars is depicted in the inset.

0.5) nm and  $d_{\text{XRD}}^{\text{CoFe-mod}} = (4.4 \pm 0.5)$  nm for the CoFe<sub>free</sub> and CoFe<sub>mod</sub> samples, respectively. Slight decrease of the  $d_{\text{XRD}}^{\text{CoFe-mod}}$  in comparison with  $d_{\text{XRD}}^{\text{CoFe-free}}$  can be explained as lowering of the NP crystallinity in the surface layer of the NP (a *shell*) and hence reduction of the size of coherently diffracting domain after the citric acid treatment.

In the case of the CoFe<sub>2</sub>O<sub>4</sub>/CeO<sub>2</sub> nanocomposite samples, the reflections corresponding to the CoFe<sub>2</sub>O<sub>4</sub> phase possess very low intensity (comparable with the background) and most of them are completely overlapped by the CeO<sub>2</sub> reflections (Figure 1(b)). Therefore, neither the presence of the CoFe<sub>2</sub>O<sub>4</sub> NPs nor the NP diameters is determinable by the PXRD. It has been observed that the CeO<sub>2</sub> matrix is

nanocrystalline in all nanocomposite samples (Figure 1(b)); resulting values of the crystallite sizes,  $d_{\text{XRD}}^{\text{CeO}_2}$ , and lattice parameters,  $a^{\text{CeO}_2}$ , are summarized in Table 1. It is obvious that  $d_{\text{XRD}}^{\text{CeO}_2}$  decreases with increasing final pH. The determined  $a^{\text{CeO}_2}$  values are in good agreement with the bulk tabulated value,  $a^{\text{CeO}_2}_{\text{bulk}} = 5.41$  Å.

In order to study the temperature stability of the CoFe<sub>2</sub>O<sub>4</sub>/CeO<sub>2</sub> nanocomposites, in situ PXRD study of the v04 sample was carried out up to 500°C. The typical patterns for three different annealing temperatures,  $T_{\text{ann}}$ , are shown in Figure 1(c). No additional phase formed during annealing process.  $d_{\text{XRD}}^{\text{CeO}_2}$  increases with increasing  $T_{\text{ann}}$

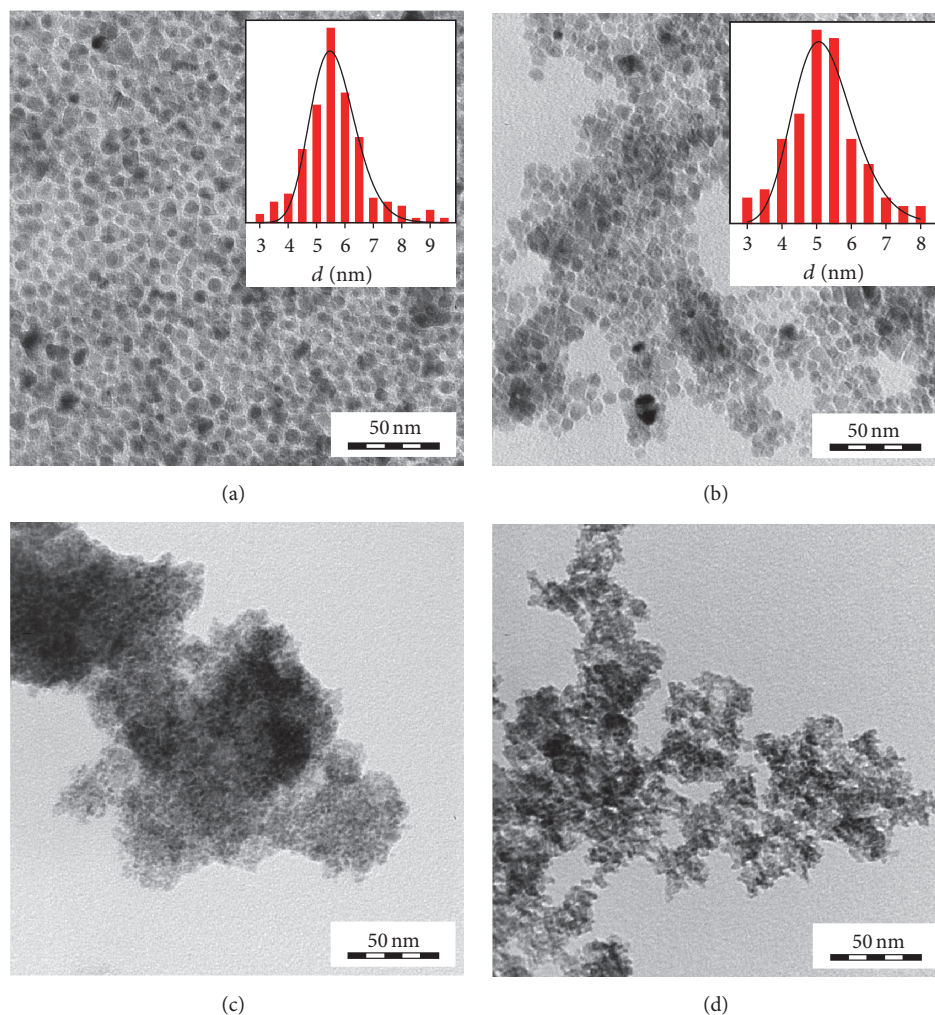


FIGURE 2: The TEM micrographs of the (a) CoFe<sub>free</sub>, (b) CoFe<sub>mod</sub>, (c) v02, and (d) v06 samples. Particle size distributions obtained from the images for the matrix-free samples are in the insets.

from  $(1.7 \pm 0.2)$  nm at  $25^\circ\text{C}$  to  $(2.1 \pm 0.2)$  nm at  $500^\circ\text{C}$  (see inset of Figure 1(c)). The observed increase of diameter of the CeO<sub>2</sub> nanocrystallites is consistent with decrease of the width of the CeO<sub>2</sub> reflections with increasing  $T_{\text{ann}}$ , as is shown in Figure 1(c). The obtained results indicate that the nanocomposite is thermally stable up to the  $500^\circ\text{C}$ .

The EDX measurements confirmed the expected elemental composition of the samples; results are summarized in Table S1 in the Supplementary Material available online at <http://dx.doi.org/10.1155/2016/7091241>. Fe and Co contents for the CoFe<sub>free</sub> sample correspond within the error to the Fe/Co ratio expected for the stoichiometric CoFe<sub>2</sub>O<sub>4</sub>. However, the CoFe<sub>mod</sub> sample contains higher amount of the Fe than the CoFe<sub>free</sub> sample with the Fe/Co ratio equal to 3.7 instead of expected stoichiometric 2. This implies that some Co is missing in the CoFe<sub>mod</sub> sample. One of the possible explanations is modification by citric acid. This can result in the formation of a Co-depleted shell.

If we assume the limiting case in which the modified NPs have the core-shell structure, with the stoichiometric CoFe<sub>2</sub>O<sub>4</sub> crystalline core and disordered Co-depleted shell, we can easily calculate the volume attributed to the shell.

Let us assume that both the CoFe<sub>free</sub> and CoFe<sub>mod</sub> samples have the same apparent size of the NPs,  $d_a$ , and apparent volume,  $V_a$ . For the NPs in the CoFe<sub>free</sub> sample,  $V_a$  corresponds to the CoFe<sub>2</sub>O<sub>4</sub> from 100%. If we compare the Fe/Co ratio for the CoFe<sub>free</sub> and CoFe<sub>mod</sub> samples (2.4 versus 3.7), then the NPs in the CoFe<sub>mod</sub> sample contain 66% of the CoFe<sub>2</sub>O<sub>4</sub>. If this CoFe<sub>2</sub>O<sub>4</sub> forms the NP core, its diameter corresponds to 82% of the CoFe<sub>free</sub> diameter. This agrees well with the results of the PXRD, where  $d_{\text{XRD}}^{\text{CoFe}_{\text{mod}}}$  corresponds only to the 94% of the  $d_{\text{XRD}}^{\text{CoFe}_{\text{free}}}$  value. Hence the partial removal of the Co from the NP shell is reasonable explanation of the changed Fe/Co ratio after the citric acid treatment.

In the case of the nanocomposite samples, the Fe/Co ratios are within the error close to the value for the CoFe<sub>mod</sub> sample (3.6–4.2, Table S1), indicating that the elemental composition of the NPs was not affected by the incorporation of the NPs into the matrix.

The NPs were directly observed by TEM. In the case of matrix-free CoFe<sub>free</sub> and CoFe<sub>mod</sub> samples, the individual NPs can be clearly distinguishable (Figures 2(a) and 2(b))

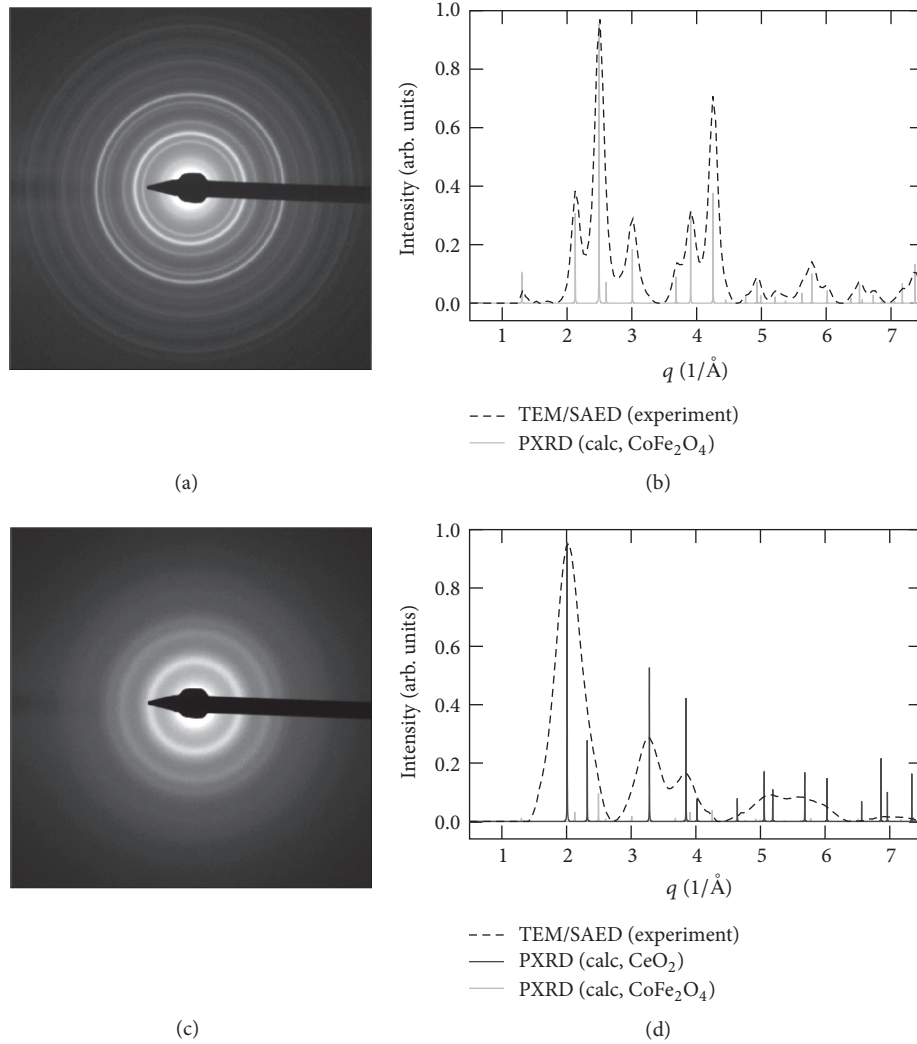


FIGURE 3: Electron diffraction results for (a, b)  $\text{CoFe}_{\text{free}}$  and (c, d) v06 samples: experimental TEM/SAED diffraction patterns (a, c) and their comparison with calculated PXRD diffractograms of  $\text{CoFe}_2\text{O}_4$  and  $\text{CeO}_2$  (b, d). We note that the intensities of the most intensive diffractions in PXRD patterns of  $\text{CoFe}_2\text{O}_4$  and  $\text{CeO}_2$  are scaled 1 : 10 due to the expected low concentration of the  $\text{CoFe}_2\text{O}_4$  in the composite.

and, as a result, the particle size distributions of these two samples were obtained (insets of the Figures 2(a) and 2(b)). The mean physical particle size determined from the particle size histograms is  $d_{\text{TEM}}^{\text{CoFe}_{\text{free}}} = (5.7 \pm 0.5) \text{ nm}$  and  $d_{\text{TEM}}^{\text{CoFe}_{\text{mod}}} = (5.3 \pm 0.5) \text{ nm}$  for the  $\text{CoFe}_{\text{free}}$  and  $\text{CoFe}_{\text{mod}}$  samples, respectively. It can be observed that  $d_{\text{TEM}}^{\text{CoFe}_{\text{free}}}$  is slightly larger than  $d_{\text{TEM}}^{\text{CoFe}_{\text{mod}}}$  as a consequence of the surface modification by citric acid. Chemical treatment connected with the surface modification probably causes partial dissolution of the NPs resulting in the observed difference between NP sizes of both samples. The morphology of the all nanocomposite samples observed by TEM and HR-TEM is comparable; representative TEM micrographs of the v02 and v06 samples are shown in Figures 2(c) and 2(d) (micrographs for other nanocomposite samples are given in Figure S1). In the nanocomposite samples, the  $\text{CoFe}_2\text{O}_4$  NPs are surrounded by smaller  $\text{CeO}_2$  NPs which makes their

observation and hence determination of the particle size distributions and mean  $d_{\text{TEM}}$  rather difficult and imprecise.

TEM/SAED experiments (Figure 3) confirmed the results of PXRD: the matrix-free NPs (Figures 3(a) and 3(b)) correspond to the  $\text{CoFe}_2\text{O}_4$  spinel structure (Crystallography Open Database [41], record ID = 5910063). In the case of  $\text{CoFe}_2\text{O}_4/\text{CeO}_2$  nanocomposite samples (Figures 3(c) and 3(d)), the diffractograms are dominated by the broad diffractions of  $\text{CeO}_2$  cubic phase (Crystallography Open Database [41], record ID = 9009008). The broad diffractions in Figures 3(c) and 3(d) are associated with the smaller size of  $\text{CeO}_2$  crystallites (width of the peak is inversely proportional to the crystallite size). Weak  $\text{CoFe}_2\text{O}_4$  diffractions form just weak shoulders of dominating  $\text{CeO}_2$  peaks, which is due to the low concentration of the  $\text{CoFe}_2\text{O}_4$  in the composite.

The BET measurements of nanocomposite samples were carried out in order to determine the specific surface area,

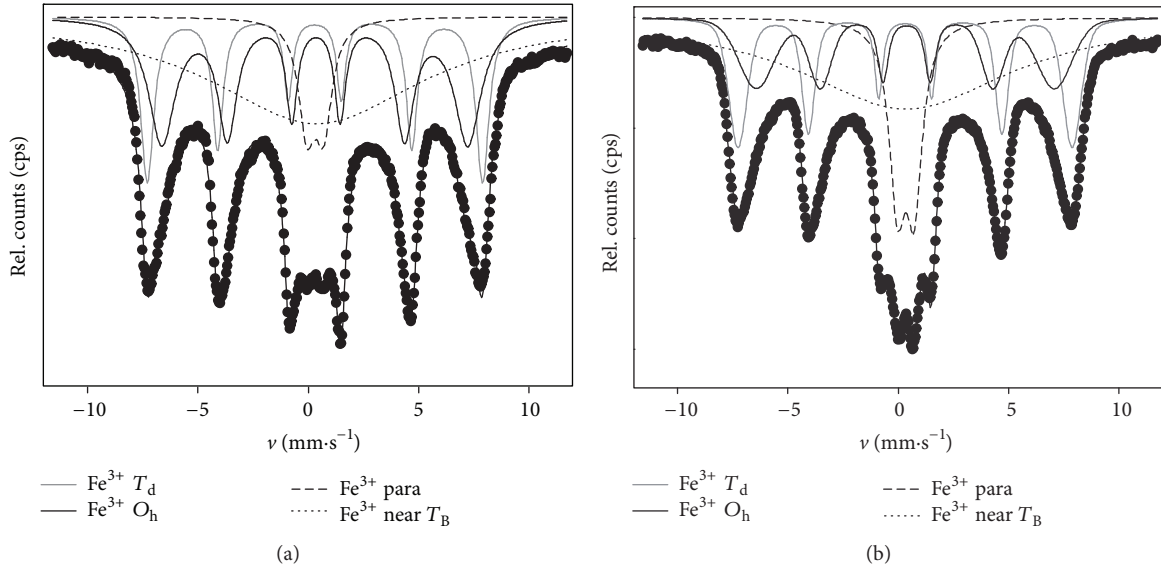


FIGURE 4: Mössbauer spectra of the CoFe\_free (a) and CoFe\_mod (b) samples performed at RT.

$S_{\text{BET}}$ , as one of the important characteristics of the nanocomposite materials. The results are summarized in Table 1. It is obvious that  $S_{\text{BET}}$  increases with increasing final pH, which is consistent with the evolution of  $d_{\text{XRD}}^{\text{CeO}_2}$  values with the preparation conditions. The resulting values of the  $S_{\text{BET}}$  are significantly higher than the values previously reported for the  $\text{CeO}_2$ -based materials [10, 12, 13, 22, 45–47]. It is also clear that  $S_{\text{BET}}$  of the v06 sample is more than 25% higher than that of the other samples. These results are in good agreement with the different morphology of the v06 sample as observed by SEM, with larger surface area. Due to very high  $S_{\text{BET}}$  values, the high catalytic activity of our samples is expected [45]. A test of catalytic performance by means of oxidation of butane to carbon dioxide in oxygen/argon atmosphere was carried out; for details see Supplementary Material.

Finally, the nature of the spinel phase in the NP samples was investigated using Mössbauer Spectroscopy. The Mössbauer spectra of the CoFe\_free and CoFe\_mod samples (Figure 4) reveal that most of the NPs are in the blocked state at RT, as is observed from the presence of sextet with asymmetric absorption peaks corresponding to the small particle size with nonzero size distribution. The doublet and singlet in the spectra correspond to the NPs in superparamagnetic (SPM) regime and are close to the blocking temperature,  $T_{\text{B}}$ , respectively. No significant changes in the spectra and Mössbauer parameters of the CoFe\_mod sample in comparison with the CoFe\_free sample indicate that the modification of the sample is not connected with remarkable structural or phase changes.

Quantitative information about samples was extracted refining all spectra; parameters of the fit and resulting Mössbauer parameters are summarized in the Supplementary Material (Table S2). The convolution of the Gaussian distribution and Lorentzian profile function was used to refine the sextet spectra. Determined smaller values of the hyperfine fields (43.0 T for the  $\text{O}_{\text{h}}$  sites and 47.2 T for the  $T_{\text{d}}$  sites of the

CoFe\_free and CoFe\_mod samples) are consistent with small  $\text{CoFe}_2\text{O}_4$   $d_{\text{XRD}}$ . The isomer shifts,  $\delta \sim 0.3 \text{ mm}\cdot\text{s}^{-1}$ , and zero quadrupole shifts are attributed to the ferrite spinel structure [25].

Slight change in the relative area of the doublet (13.6% versus 23.4% for CoFe\_free and CoFe\_mod samples, resp.) can be interpreted as the change in the NP surface layer (increase of disorder of the surface) in the CoFe\_mod sample with respect to the CoFe\_free sample after citric acid treatment.

**3.2. Magnetic Properties.** Magnetic measurements were carried out in order to unambiguously confirm the presence of the  $\text{CoFe}_2\text{O}_4$  NPs in the nanocomposites; advanced analysis of the data was applied in order to examine changes in the magnetic response of the NPs associated with their surface modification and incorporation into the  $\text{CeO}_2$  matrix.

The ZFC-FC curves of the CoFe\_free sample exhibit behavior expected for the SPM system with the interparticle interactions [48, 49] that are manifested by the saturation of the low temperature part of the FC curve (Figure 5(a)). The temperature of the maximum of the ZFC curve,  $T_{\text{MAX}}$ , reaches  $(270 \pm 2) \text{ K}$ . The ZFC-FC curves of the CoFe\_mod and nanocomposite samples are comparable to that of the CoFe\_free sample (Figure 5(b)); difference is the broader maximum at the ZFC curves of the nanocomposite samples. The values of  $T_{\text{MAX}}$  are summarized in Table 2. There is observable increase of  $T_{\text{MAX}}$  value for the CoFe\_mod sample and larger increase for the nanocomposite samples in comparison with the CoFe\_free sample. No features indicating presence of another magnetic phase except the SPM  $\text{CoFe}_2\text{O}_4$  were observed.

The ZFC curves were refined using theoretical relationship for the ZFC magnetization of the NP system [50] (details are in the Supplementary Material) in order to estimate distribution of  $T_{\text{B}}$  and to evaluate the effect of the particle size and effective anisotropy distributions. The resulting values

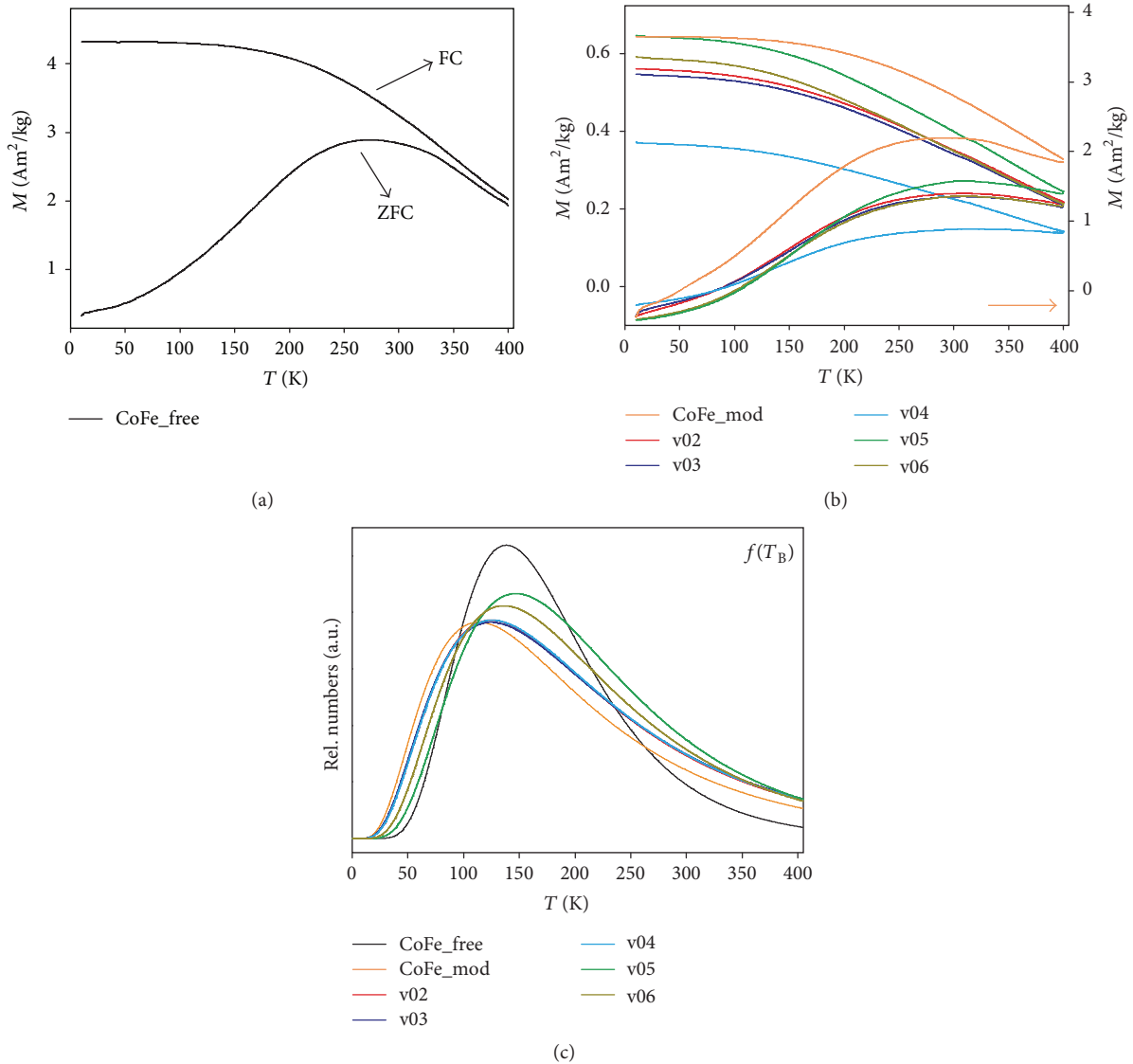


FIGURE 5: (a, b) The ZFC-FC curves measured at 0.01 T for the  $\text{CoFe}_{\text{free}}$ ,  $\text{CoFe}_{\text{mod}}$ , and  $v_0x$  samples, respectively. (c) Distribution of blocking temperatures,  $f(T_B)$ , obtained from the ZFC curve refinement (details about the data analysis can be found in the Supplementary Material).

of the mean blocking temperature,  $T_{B,\text{mean}}$ , are summarized in Table 2. Compared with the values of  $T_{B,\text{mean}}$  for the  $\text{CoFe}_{\text{free}}$  sample,  $T_{B,\text{mean}}$  increases after the NP surface modification (the  $\text{CoFe}_{\text{mod}}$  sample) and further after the incorporation of the NPs into the matrix (the nanocomposite samples). Focusing on the details of preparation, the increase of the  $T_{B,\text{mean}}$  is larger for dropwise addition of the NaOH (the  $v_02$ – $v_04$  samples,  $\sim 230$  K) than for the fast addition of the NaOH (the  $v_05$  and  $v_06$  samples,  $\sim 220$  K).

The  $T_B$  distribution for the  $\text{CoFe}_{\text{mod}}$  and nanocomposite samples is wider in comparison with the  $\text{CoFe}_{\text{free}}$  sample, but the individual distributions are comparable for the nanocomposite samples prepared with the similar rate of the NaOH addition (comparing the  $v_02$ – $v_04$  versus  $v_05$  and  $v_06$  samples, Figure 5(c)). Hence we can conclude that distribution width for the nanocomposite samples and

corresponding shift of  $T_{B,\text{mean}}$  are given by that rate of the NaOH addition.

Focusing on the mechanism behind  $T_B$  distribution widening for the  $\text{CoFe}_{\text{mod}}$  and nanocomposite samples, we can explain observed effects as follows: the process of the NP surface modification by citric acid and embedding of the NPs into the matrix can vary both the NP volume as well as its effective anisotropy constants,  $K_{\text{eff}}$ , and hence distribution of  $T_B$  as a result. The NP  $K_{\text{eff}}$  is given both by the particle volume and by the surface anisotropy constant term [48] which is significantly influenced by any changes of the NP spin structure that can arise during the modification and embedding process. In our case, the spin structure and hence the  $K_{\text{eff}}$  can be varied by at least one of the three different mechanisms: (1) Change of the particle volume and particle size distribution, which also alter  $K_{\text{eff}}$  due to

TABLE 2: Magnetic parameters of the samples: temperature of the maximum of the ZFC curve,  $T_{MAX}$  (range of error  $\sim 10$  K for nanocomposite samples due to the broad maximum); mean blocking temperature,  $T_{B,mean}$ , obtained from the fit of the ZFC curve with distribution of blocking temperatures (range of error  $\sim 2$  K); saturation magnetization at 10 and 400 K,  $M_S^{10}$  and  $M_S^{400}$  (range of error  $\sim 1$  Am<sup>2</sup>/kg); coercivity at 10 K,  $\mu_0 H_C^{10}$  (range of error  $\sim 0.05$  T); and effective anisotropy constant,  $K_{eff}$  obtained using (1) (range of error  $\sim 0.06 \times 10^6$  J/m<sup>3</sup>). Results of the refinement of the  $M(B)$  curves: mean magnetic moments,  $\mu_m$ , and corresponding mean magnetic particle diameters,  $d_{MAG}^{CoFe_2O_4}$ .

Sample	$T_{MAX}$ (K)	$T_{B,mean}$ (K)	$M_S^{10}$ (Am <sup>2</sup> /kg)	$M_S^{400}$ (Am <sup>2</sup> /kg)	$\mu_0 H_C^{10}$ (T)	$\mu_m \times 10^3$ ( $\mu_B$ )	$d_{MAG}^{CoFe_2O_4}$ (nm)	$K_{eff} \times 10^6$ (J/m <sup>3</sup> )
CoFe_free	$\sim 274$	180	67.0	45.0	1.12	$3.05 \pm 0.31$	$4.4 \pm 0.1$	1.40
CoFe_mod	$\sim 288$	211	69.0	47.0	1.08	$2.78 \pm 0.28$	$4.3 \pm 0.1$	1.75
v02	$\sim 300$	227	7.5	4.6	0.92	$2.18 \pm 0.22$	$4.0 \pm 0.1$	2.33
v03	$\sim 310$	230	7.8	4.4	0.83	$1.83 \pm 0.18$	$3.7 \pm 0.1$	2.99
v04	$\sim 320$	228	5.3	3.3	0.84	$1.78 \pm 0.18$	$3.7 \pm 0.1$	2.96
v05	$\sim 306$	224	8.1	4.1	0.81	$2.37 \pm 0.24$	$4.1 \pm 0.1$	2.14
v06	$\sim 308$	222	6.8	3.3	0.83	$2.56 \pm 0.26$	$4.2 \pm 0.1$	1.97

the finite-size effect [48]. Partial dissolution of the NPs may be the consequence of the addition of citric acid/NaOH. In the case of the nanocomposite samples, the different NaOH addition regimes theoretically lead to the different volume changes for individual samples. (2) Chemical treatment during modification and incorporation process (e.g., addition of the citric acid/NaOH) which causes surface disruptions and hence alters the surface spin structure [51, 52]. In the nanocomposite samples, each regime of the NaOH addition can lead to different degrees of surface disruptions and as a result affects  $K_{eff}$  and  $T_B$  distributions. Chemical treatment of the as-prepared NPs during their incorporation into the matrix should affect just the NP surface/shell layer, not the ion distribution within the NPs. Comparing our results with the literature, Aneesh Kumar et al. [53, 54] reported study of the role of the pH value during chemical reaction on the magnetic properties of the spinel ferrite structure. Adjusting of the pH value led to the change of the cation distribution in the spinel structure. However, in our work, the as-prepared  $CoFe_2O_4$  nanoparticles were exposed to the different pH values during the embedding process to the matrix, not during the formation of the individual nanoparticles as in the Aneesh Kumar works. Thus the degree of inversion in our  $CoFe_2O_4$  nanoparticles should not be significantly modified by changing the pH during the embedding step, as it is not expected to change cation distribution in the whole volume of the as-prepared nanoparticles by the subsequent pH treatment unlike the case of nanoparticles exposed to the pH treatment during their formation. (3) Change of the interparticle interactions can also lead to the changes in the alignment of the surface spins (the so-called spin canting). Surface modification of the NPs causes raising of the strength of the dipolar interactions via decreasing of the interparticle distances between NPs with the citric acid coatings in comparison with the oleic acid coated NPs of the CoFe\_free sample [55]. On the other hand, dispersion of the NPs in the  $CeO_2$  matrix in the case of nanocomposite samples leads to the weakening of the dipolar interparticle interactions. Both effects result in the changes of the spin structure of the NPs.

All three mechanisms leading to different width of the  $T_B$  distribution can be present simultaneously and their individual contributions are not clearly distinguishable, especially if we have no information about apparent or crystallite NP size in the nanocomposite samples. However, experimentally observed change of the NP crystalline size for the CoFe\_mod sample in comparison with the CoFe\_free sample suggests that the first and second mechanisms are reasonable for explanation of the effects after exposure of the NPs to citric acid.

The  $M(B)$  of all samples measured at 10 K are symmetric for both polarities of the magnetic field.  $M(B)$  curves measured at 400 K are unhyseretic (Figure 6) which indicates that the NPs are in the SPM regime. The determined magnetic parameters (coercivity at 10 K,  $\mu_0 H_C^{10}$ , and saturation magnetization at 10 and 400 K,  $M_S^{10}$  and  $M_S^{400}$ ) are summarized in Table 2. The CoFe\_free sample possesses very similar  $\mu_0 H_C^{10}$  value as was previously reported for the NPs prepared by hydrothermal method [29]. The CoFe\_mod sample exhibits nearly the same hysteretic behavior as the reference CoFe\_free sample (Figure 6(a)), with the similar value of  $\mu_0 H_C^{10}$  indicating presence of no other magnetic phase except the  $CoFe_2O_4$ .

All nanocomposite samples exhibit similar large  $\mu_0 H_C^{10}$  values, lower than the value for the CoFe\_free sample. Decrease of the  $\mu_0 H_C^{10}$  value can be explained by the varied  $K_{eff}$  value, modified single NP properties, or weakening of the interparticle interactions due to incorporation of the NPs into the matrix, as was already discussed in the description of the  $M(T)$  curves and  $T_B$  distributions above.

$M(B)$  curves were refined in the MINORIM software [44] to determine the distribution of the magnetic moments (superspins),  $\mu$ , belonging to the individual  $CoFe_2O_4$  NPs. Resulting fits are depicted as solid lines in Figures 6(b) (the CoFe\_free and CoFe\_mod samples) and 6(d) (nanocomposite samples). Resulting  $\mu$  distributions are shown in Figure 7. The unimodal  $\mu$  distribution was found for all samples; values of the mean magnetic moments,  $\mu_m$ , are summarized in Table 2. The mean magnetic diameters of the NPs,  $d_{MAG}^{CoFe_2O_4}$ , were

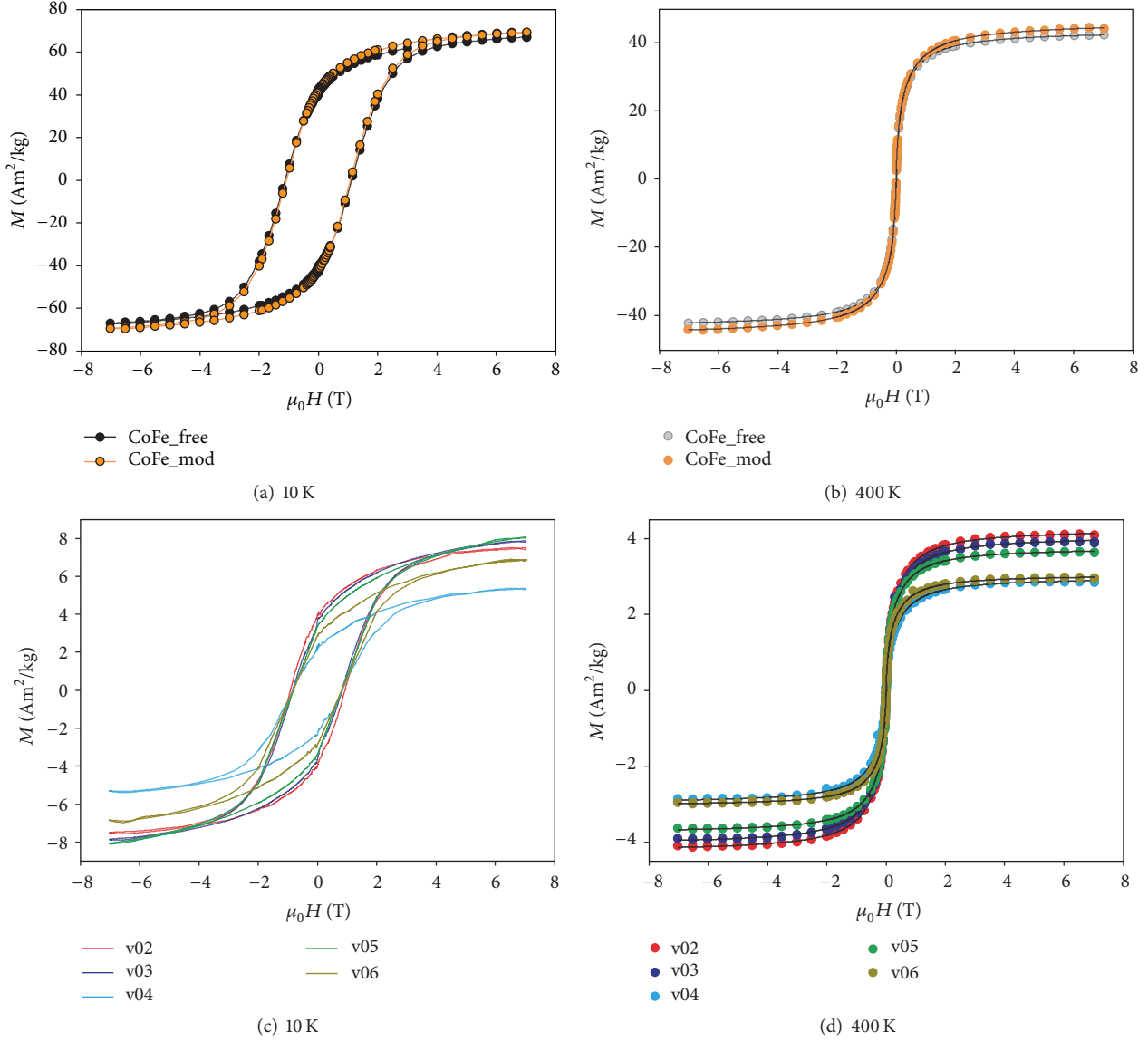


FIGURE 6: (a, b) Magnetization isotherms of the CoFe\_free and CoFe\_mod samples measured at 10 K and 400 K together with refined curves (solid lines) at 400 K. (c) Magnetization isotherms of the nanocomposite samples measured at 10 K. (d) Magnetization isotherms of the nanocomposite samples measured at 400 K together with the refined curves (solid lines).

calculated from the  $\mu_m$  values in the same way as is described in [56]. Taking the average  $\mu$  per formula unit of the half inverse  $\text{CoFe}_2\text{O}_4$  equal to  $5\mu_B$  [57] and considering that the unit cell contains eight formula units, the  $\mu$  per unit cell,  $\mu_{\text{uc}}$ , was taken as  $40\mu_B$  for all samples. The resulting values of the  $d_{\text{MAG}}^{\text{CoFe}_2\text{O}_4}$  are summarized in Table 2.

Analysis of the  $\mu$  distributions for individual samples revealed that the  $\mu$  distribution changes with the surface modification of the NPs (when the CoFe\_free and CoFe\_mod samples are compared) and then again with incorporation of the NPs into the matrix (Figure 7 and Table 2). The maximum of the  $\mu$  distribution as well as  $\mu_m$  and corresponding  $d_{\text{MAG}}^{\text{CoFe}_2\text{O}_4}$  values are shifted to the lower values after the citric acid and subsequently the NaOH treatments. Decrease of the  $d_{\text{MAG}}^{\text{CoFe}_2\text{O}_4}$  value for the CoFe\_mod sample

in comparison with the CoFe\_free sample is consistent with decreased  $d_{\text{XRD}}$  and proposed core-shell structure of the modified NPs, with the Co-free (deficit) shell. The largest reduction of the  $\mu_m$  values was observed for the samples exposed to dropwise addition of the NaOH (the v02–v04 sample series) with the highest pH value (the v04 sample). We assume that higher final pH may cause larger changes in the structure and spin order in the NP surface layer during the incorporation process resulting into the reduction of the  $d_{\text{MAG}}^{\text{CoFe}_2\text{O}_4}$  value, whereas fast addition of NaOH leads to smaller changes of the NP surface layer as the reaction is generally faster (the v05 and v06 samples). We also observed that variation of the  $d_{\text{MAG}}^{\text{CoFe}_2\text{O}_4}$  through the nanocomposite sample series is comparable with variation of the  $M_S^{10}$  values. All together finally suggest that not only the NP size and size

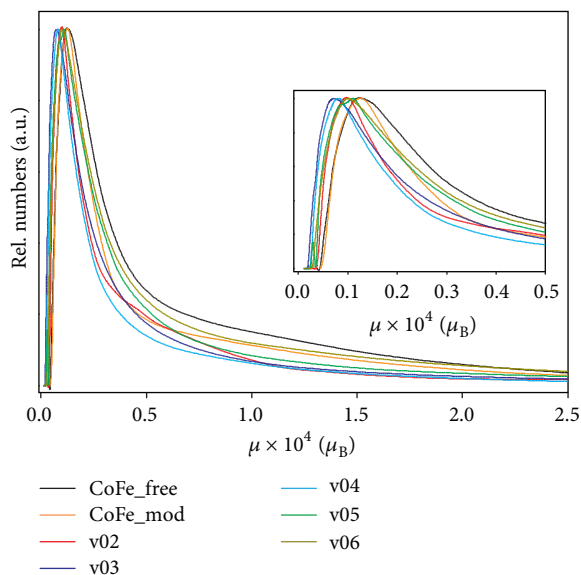


FIGURE 7: Distribution of the magnetic moments,  $\mu$ , of the samples as a result of the refinement of the  $M(B)$  curves.

distribution, but also the surface spin alignment and hence  $K_{\text{eff}}$  are slightly modified after chemical treatment of the NPs.

$K_{\text{eff}}$  of the  $\text{CoFe}_2\text{O}_4$  NPs was estimated from the values of  $T_{\text{B,mean}}$  and  $d_{\text{MAG}}^{\text{CoFe}_2\text{O}_4}$  using the relationship for  $T_{\text{B}}$  of the SPM NPs [48], resulting in the equation for  $K_{\text{eff}}$ :

$$K_{\text{eff}} = \frac{6}{\pi} \frac{25k_{\text{B}}T_{\text{B,mean}}}{\left(d_{\text{MAG}}^{\text{CoFe}_2\text{O}_4}\right)^3}. \quad (1)$$

Overall evolution of the  $K_{\text{eff}}$  values through the sample series (Table 2) is consistent with the so-called finite-size effect [48]— $K_{\text{eff}}$  increases with decreasing particle size,  $d_{\text{MAG}}^{\text{CoFe}_2\text{O}_4}$ . Its value is larger than the bulk value,  $K_{\text{eff}}^{\text{bulk}} = 1.8\text{--}2.7 \times 10^5 \text{ J/m}^3$  [27, 58], for all samples and corresponds with the value expected for the small NP (with diameter reaching approximately 4 nm).  $K_{\text{eff}}$  increases with the modification by citric acid and subsequently with the NaOH treatment, reaching the largest values for dropwise addition of NaOH under large final pH, which is consistent very well with our previous findings. These results finally confirmed previous assumptions deduced from the  $T_{\text{B}}$  and  $\mu$  distributions that  $K_{\text{eff}}$  (especially its surface term) is altered after the surface modification and incorporation of the NPs into the matrix.

#### 4. Conclusion

We succeeded in the preparation of the  $\text{CoFe}_2\text{O}_4/\text{CeO}_2$  nanocomposites by a novel two-step preparation route, which is based on embedding of the  $\text{CoFe}_2\text{O}_4$  NPs as magnetically active carriers into a catalytically active  $\text{CeO}_2$  matrix. Specific parameters of the preparation route, as the final pH of the reaction and method of its adjustment, were varied through the series in order to determine the most efficient conditions for preparation of the nanocomposite with the highest surface

area—a prerequisite for large catalytic activity. It has been observed that the microstructure of the  $\text{CeO}_2$  matrix evolves with preparation conditions; increase of the final pH and fast addition of the NaOH led to decrease of the crystallite diameter and consequently increase of the specific surface area.

The unambiguous presence of the  $\text{CoFe}_2\text{O}_4$  NPs in nanocomposite samples was confirmed by magnetic property measurements. The experiments revealed only slight changes in magnetic size and magnetic properties of the  $\text{CoFe}_2\text{O}_4$  NPs connected with the incorporation process. The best structural and magnetic parameters were observed for the nanocomposite sample prepared by fast addition of NaOH with the final pH equal to 12. This sample exhibits one of the largest values of the specific surface area reported for the  $\text{CeO}_2$ -based catalyst ( $264 \text{ g/m}^2$ ) and extremely low crystallite size of 2 nm. Our approach is thus very promising for production of ultrafine powders and nanocomposites with large specific surface area based on  $\text{CeO}_2$  and different magnetic carriers. Moreover, extension of the preparation route enables embedding of more than one type of nanoparticles, which open door for facile preparation of multicomponent catalytic materials.

#### Competing Interests

The authors declare that they have no conflict of interests.

#### Acknowledgments

This research was supported by the Grant Agency of the Czech Republic (Project no. 15-01953S). Magnetic measurements were performed in MLTL (<http://mltl.eu/>), which is supported within the program of Czech Research Infrastructures (Project no. LM2011025). Electron microscopy at the Institute of Macromolecular Chemistry was supported by Project POLYMAT LO1507 (Ministry of Education, Youth and Sports of the CR, program NPU I). The authors thank Mrs. Jirina Hromadkova for technical assistance.

#### References

- [1] G. Cao, *Nanostructures and Nanomaterials: Synthesis, Properties and Applications*, Imperial College Press, London, UK, 2004.
- [2] C. Dupas, P. Houdy, and M. Lahmani, *Nanoscience: Nanotechnologies and Nanophysics*, Springer, Berlin, Germany, 2007.
- [3] S. Komarneni, “Feature article. Nanocomposites,” *Journal of Materials Chemistry*, vol. 2, pp. 1219–1230, 1992.
- [4] S. Wei, Q. Wang, J. Zhu, L. Sun, H. Lin, and Z. Guo, “Multifunctional composite core-shell nanoparticles,” *Nanoscale*, vol. 3, no. 11, pp. 4474–4502, 2011.
- [5] V. Polshettiwar, R. Luque, A. Fihri, H. Zhu, M. Bouhrara, and J.-M. Basset, “Magnetically recoverable nanocatalysts,” *Chemical Reviews*, vol. 111, no. 5, pp. 3036–3075, 2011.
- [6] L. M. Rossi, N. J. S. Costa, F. P. Silva, and R. Wojcieszak, “Magnetic nanomaterials in catalysis: advanced catalysts for magnetic separation and beyond,” *Green Chemistry*, vol. 16, no. 6, pp. 2906–2933, 2014.

- [7] D. Zhang, C. Zhou, Z. Sun, L. Z. Wu, C. H. Tung, and T. Zhang, "Magnetically recyclable nanocatalysts (MRNCs): a versatile integration of high catalytic activity and facile recovery," *Nanoscale*, vol. 4, no. 20, pp. 6244–6255, 2012.
- [8] V. Tyrpekl, J. Poltieroová, A. G. Roca, N. Murafa, L. Szatmary, and D. Nižňanský, "Magnetically separable photocatalytic composite  $\gamma$ -Fe<sub>2</sub>O<sub>3</sub>@TiO<sub>2</sub> synthesized by heterogeneous precipitation," *Applied Surface Science*, vol. 257, no. 11, pp. 4844–4848, 2011.
- [9] L. Ai, H. Huang, Z. Chen, X. Wei, and J. Jiang, "Activated carbon/CoFe<sub>2</sub>O<sub>4</sub> composites: facile synthesis, magnetic performance and their potential application for the removal of malachite green from water," *Chemical Engineering Journal*, vol. 156, no. 2, pp. 243–249, 2010.
- [10] T. Arai, K. Maruya, K. Domen, and T. Onishi, "Strongly Adsorbed species to form linear hydrocarbons over partially reduced CeO<sub>2</sub>," *Journal of Catalysis*, vol. 141, no. 2, pp. 533–539, 1993.
- [11] P. Ji, J. Zhang, and F. Chen, "Study of adsorption and degradation of acid orange 7 on the surface of CeO<sub>2</sub> under visible light irradiation," *Applied Catalysis B: Environmental*, vol. 85, no. 3–4, pp. 148–154, 2009.
- [12] A. Trovarelli, C. De Leitenburg, M. Boaro, and G. Dolcetti, "The utilization of ceria in industrial catalysis," *Catalysis Today*, vol. 50, no. 2, pp. 353–367, 1999.
- [13] H. Bao, X. Chen, J. Fang, Z. Jiang, and W. Huang, "Structure-activity relation of Fe<sub>2</sub>O<sub>3</sub>-CeO<sub>2</sub> composite catalysts in CO oxidation," *Catalysis Letters*, vol. 125, no. 1–2, pp. 160–167, 2008.
- [14] R. Di Monte and J. Kaspar, "On the role of oxygen storage in three-way catalysis," *Topics in Catalysis*, vol. 28, no. 1, pp. 47–57, 2004.
- [15] M. Sahibzadab, B. C. H. Steelea, K. Zheng, R. A. Rudkin, and I. S. Metcalfeb, "Development of solid oxide fuel cells based on a Ce(Gd)O<sub>2-x</sub> electrolyte film for intermediate temperature operation," *Catalysis Today*, vol. 38, no. 4, pp. 459–466, 1997.
- [16] Y. I. Matatov-Meytal and M. Sheintuch, "Catalytic abatement of water pollutants," *Industrial & Engineering Chemistry Research*, vol. 37, no. 2, pp. 309–326, 1998.
- [17] A. R. Contreras, A. García, E. González et al., "Potential use of CeO<sub>2</sub>, TiO<sub>2</sub> and Fe<sub>3</sub>O<sub>4</sub> nanoparticles for the removal of cadmium from water," *Desalination and Water Treatment*, vol. 41, no. 1–3, pp. 296–300, 2012.
- [18] S. Recillas, A. García, E. González et al., "Use of CeO<sub>2</sub>, TiO<sub>2</sub> and Fe<sub>3</sub>O<sub>4</sub> nanoparticles for the removal of lead from water: toxicity of nanoparticles and derived compounds," *Desalination*, vol. 277, no. 1–3, pp. 213–220, 2011.
- [19] A. Mantlikova, J. Poltieroová, B. Bittova et al., "Stabilization of the high coercivity  $\epsilon$ -Fe<sub>2</sub>O<sub>3</sub> phase in the CeO<sub>2</sub>-Fe<sub>2</sub>O<sub>3</sub>/SiO<sub>2</sub> nanocomposites," *Journal of Solid State Chemistry*, vol. 191, pp. 136–141, 2012.
- [20] R. K. Selvan, C. O. Augustin, V. Šepelák, L. J. Berchmans, C. Sanjeeviraja, and A. Gedanken, "Synthesis and characterization of CuFe<sub>2</sub>O<sub>4</sub>/CeO<sub>2</sub> nanocomposites," *Materials Chemistry and Physics*, vol. 112, no. 2, pp. 373–380, 2008.
- [21] X. Li, X. Wang, D. Liu, S. Song, and H. Zhang, "Multifunctional nanostructures based on porous silica covered Fe<sub>3</sub>O<sub>4</sub>@CeO<sub>2</sub>-Pt composites: a thermally stable and magnetically-recyclable catalyst system," *Chemical Communications*, vol. 50, no. 54, pp. 7198–7201, 2014.
- [22] L. Xu and J. Wang, "Magnetic nanoscaled Fe<sub>3</sub>O<sub>4</sub>/CeO<sub>2</sub> composite as an efficient fenton-like heterogeneous catalyst for degradation of 4-chlorophenol," *Environmental Science & Technology*, vol. 46, no. 18, pp. 10145–10153, 2012.
- [23] R. M. Cornell and U. Schwertmann, *The Iron Oxides: Structure, Properties, Reactions, Occurrences and Uses*, John Wiley & Sons, Weinheim, Germany, 2003.
- [24] K. Yamada, S. Tobashi, and S. Ichiba, "Topotactic oxidation process from magnetite to maghemite studied by Rietveld analysis and <sup>119</sup>Sn Mössbauer spectroscopy," *Chemistry Letters*, vol. 19, no. 8, pp. 1327–1330, 1990.
- [25] E. Murad and J. H. Johnston, "Iron oxides and oxyhydroxides," in *Mössbauer Spectroscopy Applied to Inorganic Chemistry*, G. J. Long, Ed., Springer, New York, NY, USA, 1987.
- [26] R. Zboril, M. Mashlan, and D. Petridis, "Iron(III) oxides from thermal processesynthesis, structural and magnetic properties, mössbauer spectroscopy characterization, and applications," *Chemistry of Materials*, vol. 14, no. 3, pp. 969–982, 2002.
- [27] B. D. Cullity and C. D. Graham, *Introduction to Magnetic Materials*, John Wiley & Sons, New Jersey, NJ, USA, 2009.
- [28] A. Hutlova, D. Niznansky, J.-L. Rehspringer, C. Estournès, and M. Kurmoo, "High coercive field for nanoparticles of CoFe<sub>2</sub>O<sub>4</sub> in amorphous silica sol-gel," *Advanced Materials*, vol. 15, no. 19, pp. 1622–1625, 2003.
- [29] A. Repko, D. Nižňanský, and J. Poltieroová-Vejpravová, "A study of oleic acid-based hydrothermal preparation of CoFe<sub>2</sub>O<sub>4</sub> nanoparticles," *Journal of Nanoparticle Research*, vol. 13, no. 10, pp. 5021–5031, 2011.
- [30] J. K. Rajput and G. Kaur, "Synthesis and applications of CoFe<sub>2</sub>O<sub>4</sub> nanoparticles for multicomponent reactions," *Catalysis Science & Technology*, vol. 4, no. 1, pp. 142–151, 2014.
- [31] J. Tong, X. Cai, H. Wang, and C. Xia, "Efficient magnetic CoFe<sub>2</sub>O<sub>4</sub> nanocrystal catalyst for aerobic oxidation of cyclohexane prepared by sol-gel auto-combustion method: effects of catalyst preparation parameters," *Journal of Sol-Gel Science and Technology*, vol. 66, no. 3, pp. 452–459, 2013.
- [32] H. Li, Y. Zhang, S. Wang, Q. Wu, and C. Liu, "Study on nanomagnets supported TiO<sub>2</sub> photocatalysts prepared by a sol-gel process in reverse microemulsion combining with solvent-thermal technique," *Journal of Hazardous Materials*, vol. 169, no. 1–3, pp. 1045–1053, 2009.
- [33] G. Zhang, W. Xu, Z. Li, W. Hu, Y. Wang, and J. Magn, "Preparation and characterization of multi-functional CoFe<sub>2</sub>O<sub>4</sub>-ZnO nanocomposites," *Journal of Magnetism and Magnetic Materials*, vol. 321, no. 10, pp. 1424–1427, 2009.
- [34] N. Wetchakun, S. Chaiwichain, K. Wetchakun, W. Kangwan-supamonkon, B. Inceesungvorn, and S. Phanichphant, "Synthesis and characterization of novel magnetically separable CoFe<sub>2</sub>O<sub>4</sub>/CeO<sub>2</sub> nanocomposite photocatalysts," *Materials Letters*, vol. 113, pp. 76–79, 2013.
- [35] S. Kubickova, J. Plocek, A. Mantlikova, and J. Vejpravova, "Nanocomposites of monodisperse nanoparticles embedded in high-K oxide matrices—a general preparation strategy," *RSC Advances*, vol. 4, no. 10, pp. 5113–5121, 2014.
- [36] A. Goodarzi, Y. Sahoo, M. T. Swihart, and P. N. Prasad, "Aqueous ferrofluid of citric acid coated magnetite particles," *Materials Research Society Symposium Proceedings*, vol. 789, pp. 1–6, 2003.
- [37] E. Cheraghipour, S. Javadpour, and A. R. Mehdizadeh, "Citric capped superparamagnetic iron oxide nanoparticles used for hyperthermia therapy," *Journal of Biomedical Science and Engineering*, vol. 5, pp. 715–719, 2012.

- [38] P. C. Morais, R. L. Santos, A. C. M. Pimenta, R. B. Azevedo, and E. C. D. Lima, "Preparation and characterization of ultra-stable biocompatible magnetic fluids using citrate-coated cobalt ferrite nanoparticles," *Thin Solid Films*, vol. 515, no. 1, pp. 266–270, 2006.
- [39] J. Rodríguez-Carvajal, "Recent advances in magnetic structure determination by neutron powder diffraction," *Physica B: Condensed Matter*, vol. 192, no. 1-2, pp. 55–69, 1993.
- [40] J. L. Labár, "Consistent indexing of a (set of) single crystal SAED pattern(s) with the ProcessDiffraction program," *Ultra-microscopy*, vol. 103, no. 3, pp. 237–249, 2005.
- [41] S. Grazulis, D. Chateigner, R. T. Downs et al., "Crystallography open database—an open-access collection of crystal structures," *Journal of Applied Crystallography*, vol. 42, no. 4, pp. 726–729, 2009.
- [42] W. Kraus and G. Nolze, "POWDER CELL—a program for the representation and manipulation of crystal structures and calculation of the resulting X-ray powder patterns," *Journal of Applied Crystallography*, vol. 29, pp. 301–303, 1996.
- [43] U. Kostiv, O. Janoušková, M. Šlouf et al., "Silica-modified monodisperse hexagonal lanthanide nanocrystals: synthesis and biological properties," *Nanoscale*, vol. 7, no. 43, pp. 18096–18104, 2015.
- [44] J. Van Rijssel, B. W. M. Kuipers, and B. H. Erné, "Non-regularized inversion method from light scattering applied to ferrofluid magnetization curves for magnetic size distribution analysis," *Journal of Magnetism and Magnetic Materials*, vol. 353, pp. 110–115, 2014.
- [45] N. Laosiripojana and S. Assabumrungrat, "The effect of specific surface area on the activity of nano-scale ceria catalysts for methanol decomposition with and without steam at SOFC operating temperatures," *Chemical Engineering Science*, vol. 61, no. 8, pp. 2540–2549, 2006.
- [46] M. Luo, J. Ma, J. Lu, Y. Song, and Y. Wang, "High-surface area CuO–CeO<sub>2</sub> catalysts prepared by a surfactant-templated method for low-temperature CO oxidation," *Journal of Catalysis*, vol. 246, no. 1, pp. 52–59, 2007.
- [47] N. Laosiripojana and S. Assabumrungrat, "Catalytic steam reforming of ethanol over high surface area CeO<sub>2</sub>: The role of CeO<sub>2</sub> as an internal pre-reforming catalyst," *Applied Catalysis B: Environmental*, vol. 66, no. 1-2, pp. 29–39, 2006.
- [48] M. Knobel, W. C. Nunes, L. M. Socolovsky, E. De Biasi, J. M. Vargas, and J. C. Denardin, "Superparamagnetism and other magnetic features in granular materials: a review on ideal and real systems," *Journal of Nanoscience and Nanotechnology*, vol. 8, no. 6, pp. 2836–2857, 2008.
- [49] D. Peddis, C. Cannas, A. Musinu, and G. Piccaluga, "Magnetism in nanoparticles: beyond the effect of particle size," *Chemistry—A European Journal*, vol. 15, no. 32, pp. 7822–7829, 2009.
- [50] M. F. Hansen and S. Morup, "Estimation of blocking temperatures from ZFC/FC curves," *Journal of Magnetism and Magnetic Materials*, vol. 203, no. 1-3, pp. 214–216, 1999.
- [51] E. Umut, "Surface modification of nanoparticles used in biomedical applications," in *Modern Surface Engineering Treatments*, M. Aliofkhaezrai, Ed., InTech, Rijeka, Croatia, 2013.
- [52] D. Peddis, F. Orrù, A. Ardu, C. Cannas, A. Musinu, and G. Piccaluga, "Interparticle interactions and magnetic anisotropy in cobalt ferrite nanoparticles: influence of molecular coating," *Chemistry of Materials*, vol. 24, no. 6, pp. 1062–1071, 2012.
- [53] K. S. Aneesh Kumar and R. N. Bhowmik, "Micro-structural characterization and magnetic study of Ni<sub>1.5</sub>Fe<sub>1.5</sub>O<sub>4</sub> ferrite synthesized through coprecipitation route at different pH values," *Materials Chemistry and Physics*, vol. 146, no. 1-2, pp. 159–169, 2014.
- [54] K. S. Aneesh Kumar, R. N. Bhowmik, and S. H. Mahmood, "Role of pH value during chemical reaction, and site occupancy of Ni<sup>2+</sup> and Fe<sup>3+</sup> ions in spinel structure for tuning room temperature magnetic properties in Ni<sub>1.5</sub>Fe<sub>1.5</sub>O<sub>4</sub> ferrite," *Journal of Magnetism and Magnetic Materials*, vol. 406, pp. 60–71, 2016.
- [55] A. Repko, J. Vejpravova, T. Vackova, D. Zakutna, and D. Niznasky, "Oleate-based hydrothermal preparation of CoFe<sub>2</sub>O<sub>4</sub> nanoparticles, and their magnetic properties with respect to particle size and surface coating," *Journal of Magnetism and Magnetic Materials*, vol. 390, pp. 142–151, 2015.
- [56] B. Bittova, J. Poltieroja Vejpravova, M. Kalbac et al., "Magnetic properties of iron catalyst particles in HiPco single wall carbon nanotubes," *Journal of Physical Chemistry C*, vol. 115, no. 35, pp. 17303–17309, 2011.
- [57] Y. H. Hou, Y. J. Zhao, Z. W. Liu et al., "Structural, electronic and magnetic properties of partially inverse spinel CoFe<sub>2</sub>O<sub>4</sub>: A First-principles Study," *Journal of Physics D: Applied Physics*, vol. 43, no. 44, Article ID 445003, 2010.
- [58] V. A. M. Brabers, "Progress in spinel ferrite research," in *Handbook of Magnetic Materials*, K. H. J. Bushow, Ed., vol. 8, chapter 3, p. 212, Elsevier, Amsterdam, Netherlands, 1995.



**Hindawi**

Submit your manuscripts at  
<http://www.hindawi.com>

